Where is the unmatched transition metal in substoichiometric diboride line compounds?

Justinas Palisaitis*[1], Martin Dahlqvist[1], Allen J. Hall[2], Jimmy Thörnberg[1], Ingemar Persson[1], Nils Nedfors[1], Lars Hultman[1], Joseph E Greene[1,2,3], Ivan Petrov[1,2,3], Johanna Rosen[1] and Per O.Å. Persson[1]

[1]Thin Film Physics Division, Department of Physics, Chemistry and Biology (IFM), Linköping University, SE-581 83 Linköping, Sweden

[2] Frederick Seitz Materials Research Laboratory and Department of Materials Science, University of Illinois, Urbana, Illinois 61801, USA

[3] Department of Materials Science and Engineering, National Taiwan University of Science and Technology, Taipei 10607, Taiwan

**Corresponding author: justinas.palisaitis@liu.se*

Keywords:

Titanium diboride, line compound, substoichiometric, planar defects, high-resolution scanning transmission electron microscopy, epitaxy

Abstract

The atomic structure and local composition of high quality epitaxial substoichiometric titanium diboride ($TiB_{1.9}$) thin film, deposited by unbalanced magnetron sputtering, were studied using analytical high-resolution scanning transmission electron microscopy, density functional theory and image simulations. The unmatched Ti is pinpointed to planar defects on $\{1\bar{1}00\}$ prismatic planes and attributed to the absence of B between Ti planes that locally relaxes the structure. This mechanism allows the line compound to accommodate the off-stoichiometry and remain a line compound between defects. The planar defects are embedded in otherwise stoichiometric TiB_2 and are delineated by insertion of dislocations. An accompanied decrease in Ti-Ti bond lengths along and across the faults is observed.

Introduction

In the search for novel coating materials that are capable of withstanding harsh environments and extreme conditions while maintaining stable phase structures, increased attention has been devoted to exploring transition metal boride compounds. Titanium diboride (TiB_2) is regarded as an outstanding ceramic material that possess an excellent thermal stability, high electrical conductivity, high melting temperature, chemical inertness, and resistance to mechanical wear [1,2,3,4]. These unique properties make thin films and coatings of TiB_2 and its alloys (e.g., $Ti_{1-x}Al_xB_2$) highly attractive for a range of applications in erosive, abrasive, corrosive and high-temperature environments [5,6,7]. For example, diboride nanostructures in combination with a compressive residual stress give rise to superhardness, with values exceeding 40 GPa [2].

Regretfully, the technology for depositing diboride alloys onto e.g., tools is today limited due to challenges in the coating process. While TiB_2 constitute an extremely hard and stable ceramic, its brittleness and high elastic modulus compromises the performance when combined

with a softer substrate, like steel [8]. Consequently design and synthesis of TiB_2 coatings and thin films with performance-tailored microstructure and stoichiometry is required.

Currently, magnetron sputtering from a TiB_2 compound target is the primary approach for depositing TiB_2 thin films [9,10,11,12] although other techniques such as high-power impulse magnetron sputtering [13,14,15,16], and cathodic-arc evaporation have been addressed [17,18]. Independent of the deposition method, synthesized TiB_2 thin films typically exhibits a nanocolumnar microstructure with pronounced (0001) texture and are highly overstoichiometric in boron (TiB_{2+x}), where the excess boron segregates to the nanocolumnar grain boundaries during deposition where it forms a softening B-rich amorphous tissue phase [19,20,21].

By optimization of the deposition process and improved control the B/Ti ratio in the thin films [22,23,24], near-stoichiometric and stoichiometric TiB_2 thin films have been verified [16,25,26]. With increasing control of the stoichiometry in the wide range, synthesis of substoichiometric diborides ($TiB_{2-x)}$ were also attempted [24,27].

Little is, however, known about the atomic structure of transition metal diborides and how these line compounds manage substoichiometry of B. Formation of point defects during the sputtering process is well known and would be a means to accommodate substoichiometry on the B site. While line compounds do not permit point defects, it has been theoretically shown that introduction of isolated B-vacancies in the TiB_2 crystal structure has a destabilizing effect on the phase stability and structure due to occupation of B–B antibonding orbitals and resulting increase in states at the Fermi level [28].

To identify the mechanism by which the unmatched Ti atoms are included in the growing film, we here investigate in detail the microstructure of high quality epitaxial substoichiometric $TiB_{1.9}$ thin films by high-spatial resolution scanning transmission electron microscopy

(HRSTEM) and electron energy-loss spectroscopy spectrum imaging (EELS-SI). The experimental findings are verified using density functional theory (DFT) calculations and HRSTEM image simulations. This approach has enabled us to identify that the excess Ti atoms can be associated with planar defects in the thin film. We also identify that this mechanism is universal and applies to the formation of known phases including TiB and Ti_3B_2. Therefore, the present investigation fundamentally reveals a general atomic scale mechanism for accommodating substoichiometric diboride.

Experimental details

TiB_x thin films, ~ 0.38 μm thick, were grown on electrically-floating Al_2O_3 (0001) substrates from a TiB_2 target in a load-locked ultra-high vacuum stainless-steel dc magnetron sputter deposition system with a base pressure of $5x10^{-10}$ Torr. The magnetron was magnetically-unbalanced with the outer pole stronger than the inner pole. This configuration aided the field of the outer magnetron pole in order to controllably focus the plasma at the substrate and thus vary the plasma density and the ion flux impinging at the film-growth surface as well as the B/Ti ratio. Growth took place in Ar (99.999% pure) discharges at a constant dc power of 100 W for 40 min with a target-to-substrate separation of 6.5 cm. The substrate temperature was maintained constant at T_s = 900 ºC. The Ar pressure P_{Ar} is 20 mTorr with $\overline{B}_{axial} = (\overline{B}_{mag} + \overline{B}_{ext})$ set to 200 G and the ion to Ti flux ratio of 52 and the ion energy ~8 eV as described elsewhere [16].

B/Ti ratio in as-deposited thin films was determined from RBS analyses to be 1.9±0.04. The probe beam consists of 2 MeV He^+ ions incident normal to the sample surface with the detector set at a 150 º scattering angle. RBS spectra were analysed using the SIMNRA program [29]. Oxygen concentration was determined to be below 1 at.% by X-ray photoelectron spectroscopy (XPS) using a Kratos Analytical AXIS Ultra DLD instrument with monochromatic Al Kα

radiation (hν = 1486.6 eV); the x-ray anode was operated at 150 W. XPS sensitivity factors were obtained from absolute TiB_x compositions, determined by elastic recoil detection analyses (ERDA). XRD ω-2θ scans are obtained using a Philips X'pert MRD diffractometer operated with CuKα radiation (wavelength λ = 0.154180 nm), a Ni filter to remove CuKβ reflections, and thin-film parallel-plate collimator secondary optics. XRD scan collected in the range from 10-110 °2θ exhibits only sharp 001 and 002 003 TiB_2 reflections, indicating high quality epitaxy (see Fig. S1).

For STEM analysis, cross-sectional TEM samples were prepared using a focus ion beam (FIB) lift-out technique employing a Carl Zeiss Cross-Beam 1540 EsB system. Plan-view TEM samples were prepared by a combined approach, which includes mechanical cutting, cleaving, and polishing to few hundred μm thickness from the substrate side. The samples were fixed to the Cu grid and final milling was performed by FIB to achieve electron transparency.

The thin film sample microstructure and elemental distribution were explored at the atomic scale using high angle annular dark field STEM (HAADF-STEM) imaging, selective area electron diffraction (SAED) and electron energy-loss spectroscopy (EELS) techniques. Characterization was performed using the Linköping double Cs corrected FEI Titan^3 60-300 operated at 300 kV. HAADF-HRSTEM imaging was performed by using a 21.5 mrad convergence semi-angle which provided sub-Ångstrom resolution probes with ~ 60 pA beam current. The HAADF-STEM images were recorded using an angular detection range of 46-200 mrad. STEM-EELS spectrum images of 32x32 pixels were acquired for 1 min using a 0.25 eV/channel energy dispersion, 0.2 s pixel dwell time and a collection semi-angle of 55 mrad of the employed Gatan GIF Quantum ERS post-column imaging filter. Elemental B and Ti distribution maps were extracted from EELS spectrum images by background subtraction, using a power law, and choosing characteristic edges B-K (188-208 eV) and Ti-L_{23} (455-470 eV) energy loss integration windows.

HAADF-HRSTEM multislice image simulations were carried out using the code developed by Barthel [30]. Electron optical parameters previously listed, including aberrations up to the 3rd order were implemented in the simulations and the frozen phonon approximation was employed to account for vibrational effects. Atomic model supercells of the defect structures derived from our *ab initio* calculations were constructed using CrystalMaker 9.5.1 [31].

All first-principles calculations were performed by means of density functional theory (DFT) and the projector augmented wave method [32, 33], as implemented within the Vienna *ab-initio* simulation package (VASP) version 5.4.1 [34,35,36]. The generalized gradient approximation (GGA) as parameterized by Perdew–Burke–Ernzerhof (PBE) [37] was used for treating the electron exchange and correlation effects. A plane-wave energy cut-off of 400 eV was used and the Brillouin zone was integrated by Monkhorst–Pack special k-point sampling with a density of 0.1 $Å^{-1}$ [38]. The total energy is minimized through (i) keeping everything static, (ii) only relaxation of internal atomic positions, and (iii) relaxation of unit-cell shape, volume, and internal atomic positions until satisfying an energy convergence of 10^{-7} eV/atom and force convergence of 10^{-2} eV/Å.

The thermodynamic stability has been investigated at 0 K with respect to decomposition into any combination of competing phases. The set of most competing phases at given composition (see Table S1), also known as equilibrium simplex, is identified using a linear optimization procedure [39,40]. The stability of a phase is quantified in terms of the formation enthalpy ΔH_{cp} by comparing its energy to the energy of the equilibrium simplex according to

$$\Delta H_{cp} = E(TiB_{2-x}) - E\ (equilibrium\ simplex). \qquad (1)$$

A phase is concluded stable when $\Delta H_{cp} < 0$.

In addition, the B vacancy formation energy expressed as energy change per defect created was calculated using

$$\Delta E_{vac}=[E(TiB_{2-x})-E(TiB_2)+xE(B)]/x, \quad (2)$$

where $E(TiB_{2-x})$, $E(TiB_2)$ and E(B) is the total energy per formula unit for TiB_{2-x}, TiB_2 and B, respectively.

Results and discussion

Electron microscopy was performed on a substoichiometric $TiB_{1.9}$ thin film. The resulting overview cross-sectional (along [11$\bar{2}$0]) and plan-view (along [0001]) HAADF-STEM images together with corresponding SAED patterns (shown in the insets) are displayed in Fig. 1a and 1b, respectively.

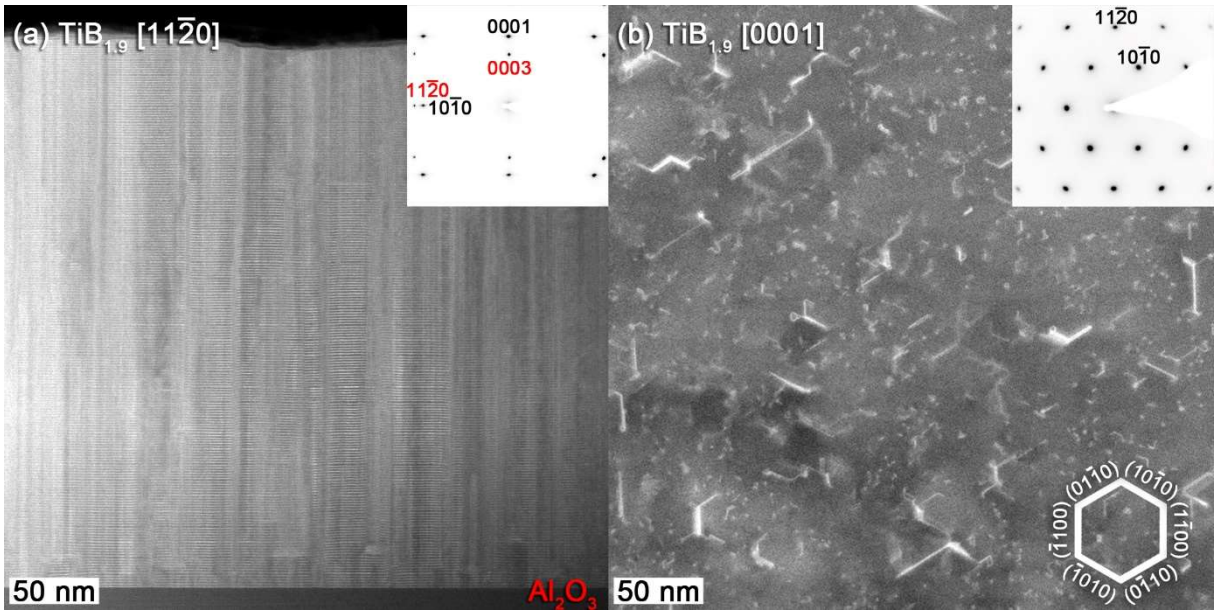

Fig. 1: *Overview HAADF-STEM images showing the microstructure of a substoichiometric $TiB_{1.9}$ thin film along the (a) cross-sectional [11$\bar{2}$0] and (b) plan-view [0001] zone axis, respectively. The insets in (a) and (b) show corresponding SAED patterns. The substrate notations are colour coded red to separate it from the thin film.*

The cross-sectional view (Fig. 1a) reveals a homogeneous thin film, which poses a near-uniform thickness of ~380 nm. The thin film exhibits a dense microstructure with a high number of column-like boundaries reaching from the thin film / substrate interface to the top of the thin

film. The width between the apparent boundaries vary in the range of ~5-30 nm, while remaining constant throughout the thin film thickness as well as perpendicular to the substrate surface. Cross-sectional HAADF-HRSTEM imaging further reveals that the lattice is locally mis-orientated (atomic-column contrast sharpness is varying in the field of view), but continues throughout the columnar-like boundaries as shown in Fig. S2.

The SAED pattern from the thin film in Fig. 1a, reveals discrete diffraction spots that indicate a high-crystal quality and firm epitaxial relationship to the underlying substrate. According to the SAED pattern, the substoichiometric $TiB_{1.9}$ thin film is oriented with the *c*-axis perpendicular to the Al_2O_3 substrate surface ($[0002]TiB_{1.9}//[0006]Al_2O_3$) and the in-plane relation $[11\bar{2}0]TiB_{1.9}//[1\bar{1}00]Al_2O_3$ in agreement with XRD results.

In the plan-view (Fig. 1b), the thin film exhibits planar-like defects with the dimensions reaching few tens on nm in size. From this low magnification image, it is clear that straight sections of the defects are aligned in a well-defined set of planes that repeat throughout the thin film. Typically, each defect is composed from a chain of sections that vary in length and width with angles between sections being 60º or 120º.

The plan-view SAED pattern in Fig. 1b further accentuates the high-crystal quality by the discrete hexagonal pattern, which is expected from a hexagonal TiB_2 crystal structure along the [0001] zone axis. Exploiting the relative orientation between the SAED pattern with respect to the defects, it is found that the defects are residing on the $\{1\bar{1}00\}$ prismatic planes of the TiB_2 crystal structure (as shown by schematics in Fig. 1b).

For further studies, it is apparent that the plan-view (Fig. 1b) is the preferred projection as it enables examination of individual defects that are projected along their extension through the TEM sample.

To elucidate the atomic structure, shape, confinement and crystallographic relationship of the planar defects with respect to the TiB_2 surrounding lattice, plan-view HAADF-HRSTEM imaging was performed and the results are shown in Fig. 2.

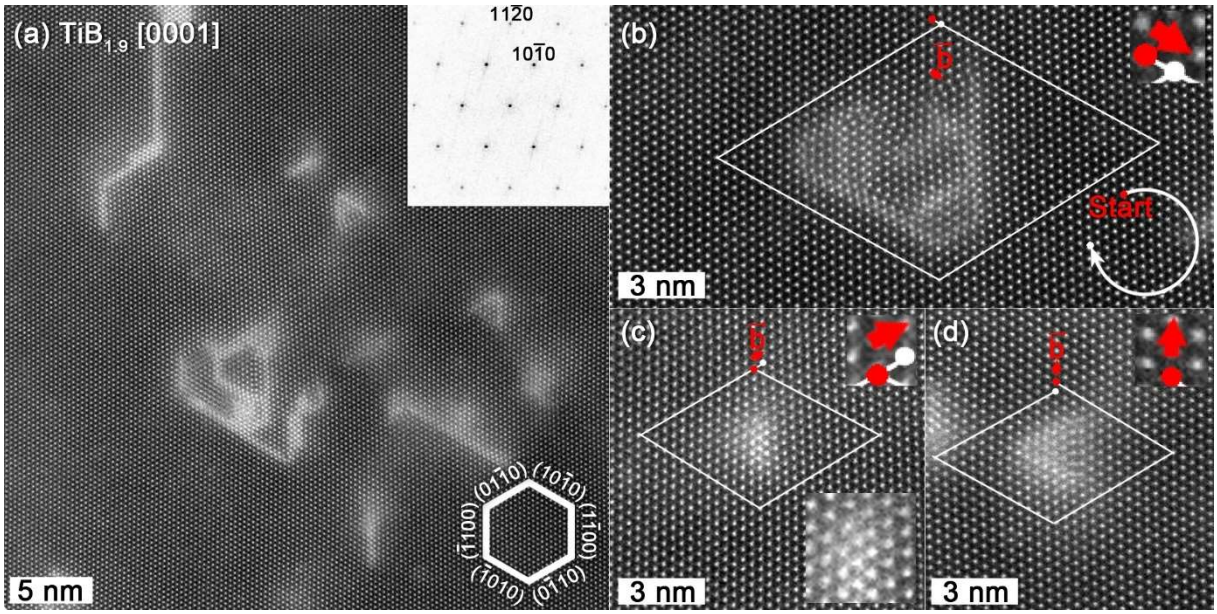

Fig. 2: *Plan-view HAADF-HRSTEM images acquired from the $TiB_{1.9}$ thin film along the [0001] zone axis together with corresponding FFT pattern in the inset. (b)-(d) the right-hand Burgers circuits drawn around the defects, Burgers vector indicated by an arrow.*

As can be seen in the plan-view image, in Fig. 2a, the defects are embedded into the thin film's crystal structure where they exhibit atomically sharp confinements with the surrounding TiB_2 lattice confirming their planar nature, with some variation in appearance, configuration and structure. The planar defects reside precisely onto the $\{1\bar{1}00\}$ prismatic planes of the TiB_2 crystal structure. The widths, of the straight portions of the planar defects, are confined to two or three Ti atomic planes, which makes them the smallest building blocks of the defect type.

Burgers circuit analysis of representative and isolated planar defects of various sizes, is shown in Fig. 2b-d. The mapped out right-hand Burger circuits failed to close completely around such

planar defects proving their association with an edge dislocation. The lattice plane discontinuity is particularly visible edge-on in the lower inset of Fig. 2c. Here, the dislocation core is clearly resolved as a result of its alignment with the electron beam. The edge dislocations are identified along the <11$\bar{2}$0> family of projected directions with a Burgers vector $\vec{b}$ = a<11$\bar{2}$0>. In combination with the cross-sectional HAADF-HRSTEM imaging (Fig. S2), the observations enable us to conclude that the dislocation exhibit edge character and extend throughout the thin film thickness (Fig. 1a).

From the three different Burgers circuits drawn in Fig. 2b-d, it can be seen that the entire family of projected directions for the edge dislocation are present. Presumably, all edge dislocations cancel out across the sample surface. This observation leads us to propose that the planar defects do not necessarily form at already nucleated edge dislocations, but that the formation of a planar defects requires nucleation of edge dislocations.

In order to access the compositional nature of the planar defects, STEM-EELS spectrum imaging was performed, and the results are shown in Fig. 3.

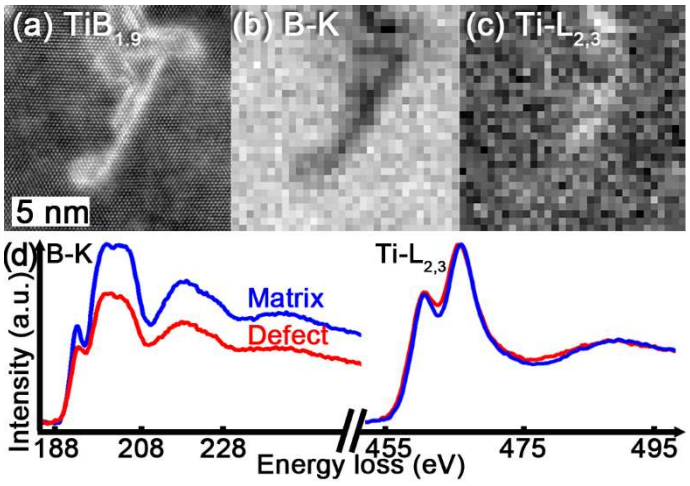

Fig. 3: *(a) Plan-view HAADF-STEM image of the planar defect which was mapped out using EELS. Background-subtracted and integrated (b) B-K (188-208 eV) and (c) Ti-L_{23} (455-470*

eV) EELS edge intensity distribution maps. (d) Core-loss EELS spectra extracted from the diboride matrix and defect areas.

Background-subtracted elemental distribution maps of the boron (B-K) and titanium (Ti-$L_{2,3}$) obtained from the planar defect area in Fig. 3a are shown in Fig. 3b-c, respectively. The obtained results reveal that the planar defects are deficient in boron and slightly enriched in titanium when compared to the ambient TiB_2. Further, extracted boron and titanium elemental edges are shown in Fig. 3d revealing the intensity and fine structure differences between the planar defect and surround crystal. The actual B content inside the planar defect is difficult to address, since the recorded (reduced) B-K signal at the defect has contribution also from adjacent B planes, hence the B content in the defect is lower. Given the line compound nature of the TiB_2 structure, it is presumed that no B exists in the plane of the defect such that it entirely consists of Ti.

In order to theoretically investigate the planar defects observed in $TiB_{1.9}$ thin film (Fig. 2), atomic models of the defects were created according to experimental observations. The models consider planar defects confined to two Ti (single-plane for B vacancies) and three Ti (double-plane for B vacancies) atomic planes. It accounts for (i) only vacancy creation or (ii) vacancy creation and an additional half unit cell shift of selected atoms under static and relaxed conditions. To ensure that a planar defect is isolated, considered unit cells have been expanded 20 to 40 times in-plane along the $[1\bar{1}00]$ direction as illustrated in Fig. 4 and Fig. S3 with a resulting planar defect separation by 25 to 50 Å without any quantitative difference.

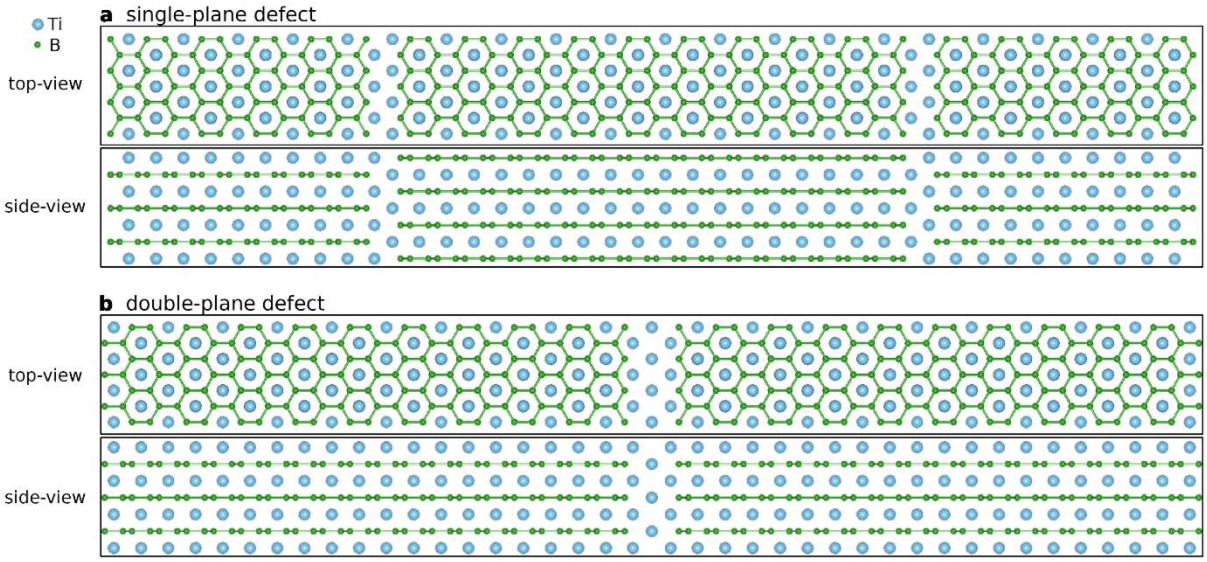

Fig. 4: *Schematic illustration of (a) two single-plane and (b) one double-plane defects for B vacancies in* $TiB_{1.9}$ *projected along* [0001] *(top-view) and* $[1\bar{1}00]$ (side-view) *directions. The unit cells expand ~103 Å in plane along* $[1\bar{1}00]$ *direction.*

Fig. 5 illustrates the stepwise change in structure and energy for single and double planes for B vacancies in $TiB_{1.9}$.

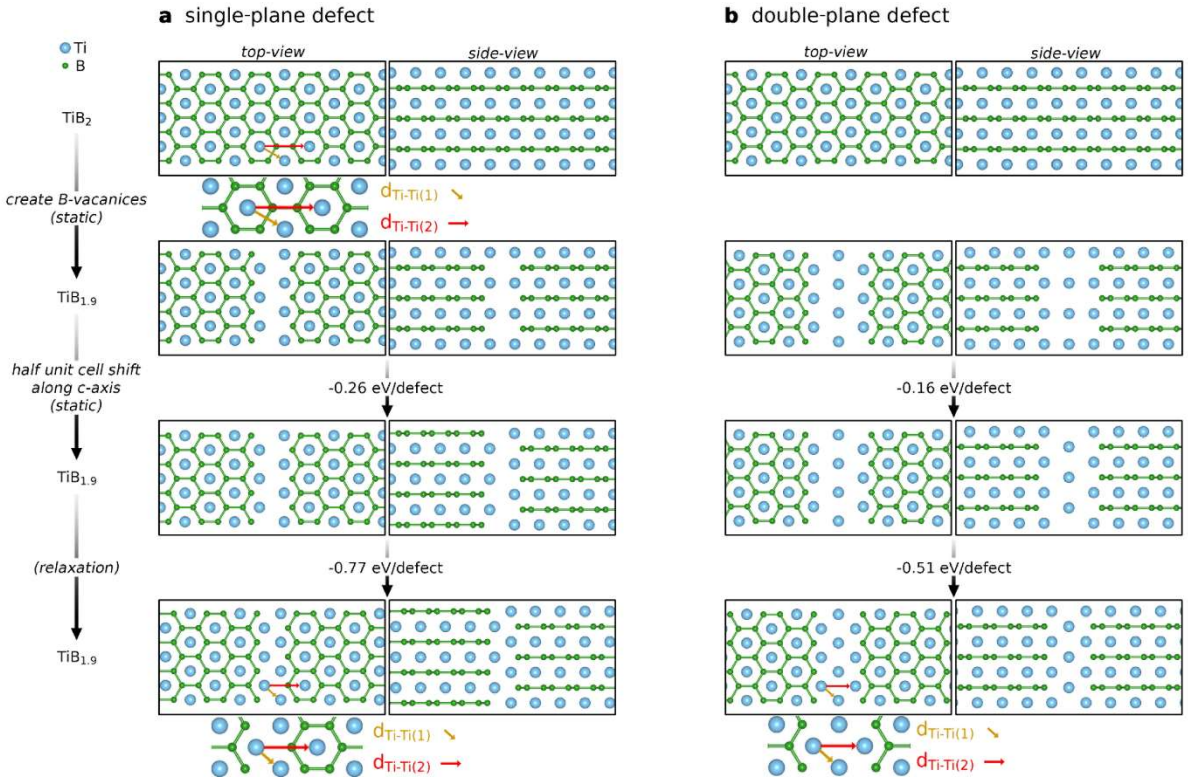

Fig. 5: *Step wise schematic illustration of (a) single plane and (b) double plane defects for B vacancies in* $TiB_{1.9}$ *projected along* [0001] *(top-view) and* [$1\bar{1}00$] (side-view) *directions. The calculated energy change for each step is given per defect (vacancy) for* $TiB_{1.9}$*. Yellow and red arrows indicate two different Ti-Ti bond lengths in the defect region.*

The calculated stability for single and double planar defects in TiB_{2-x}, see Fig. 6a, clearly indicates that both single and double planar defects are stable or close to stable only when half a unit cell is shifted (for single B plane) or Ti atoms is shifted (for double B plane). Here the identified equilibrium simplex is TiB_2 and Ti_3B_4. This can be compared to the considered case of a disordered distribution of B-vacancies, see inset in Fig. 6a, which is far from stable.

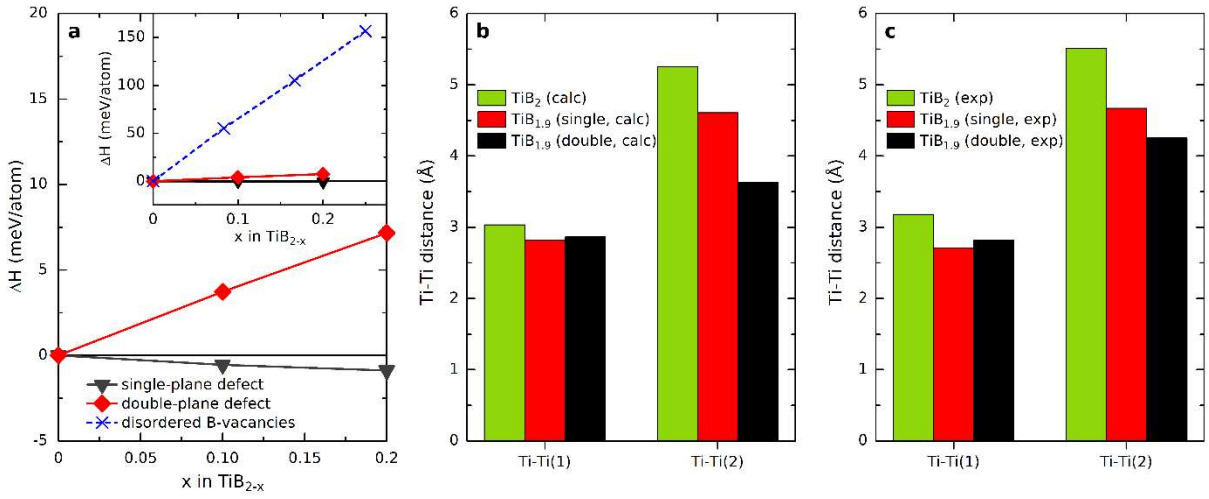

Fig. 6: *(a) Calculated stability for single- and double-plane defects for B vacancies in* TiB_{2-x} *as function of x (x=0-0.2). Inset shows calculated stability including disordered B-vacancies in* TiB_{2-x}*. (b) Two Ti-Ti distances calculated for* TiB_2 *and single- and double-plane defects in* $TiB_{1.9}$*. (c) Two Ti-Ti distances experimentally obtained from HAADF-HRSTEM images for* TiB_2 *and single- and double-plane defects in* $TiB_{1.9}$*.*

The calculated bond length for two Ti-Ti distances, Ti-Ti(1) and Ti-Ti(2), in TiB_2 and $TiB_{1.9}$ (single- and double-plane), see Fig. 6b, shows that the most notable difference between $TiB_{1.9}$ and TiB_2 are expected to observed for Ti-Ti(2). The bonds are defined in bottom of Fig. 5. This

can be compared to experimentally obtained distance obtained (from HRSTEM-HAADF images) presented in Fig. 6c.

HAADF-HRSTEM image simulations were performed to verify the defect models. Input for the HRSTEM image simulations were the fully relaxed models shown in Fig. 5. Fig. 7 shows defects' model atomic structures, the experimentally obtained and corresponding simulated HAADF- HRSTEM viewed along the [0001] zone axis. From the images, there is a qualitative agreement between the HAADF-HRSTEM experimental and simulations that confirms the proposed atomic structure model of the defect.

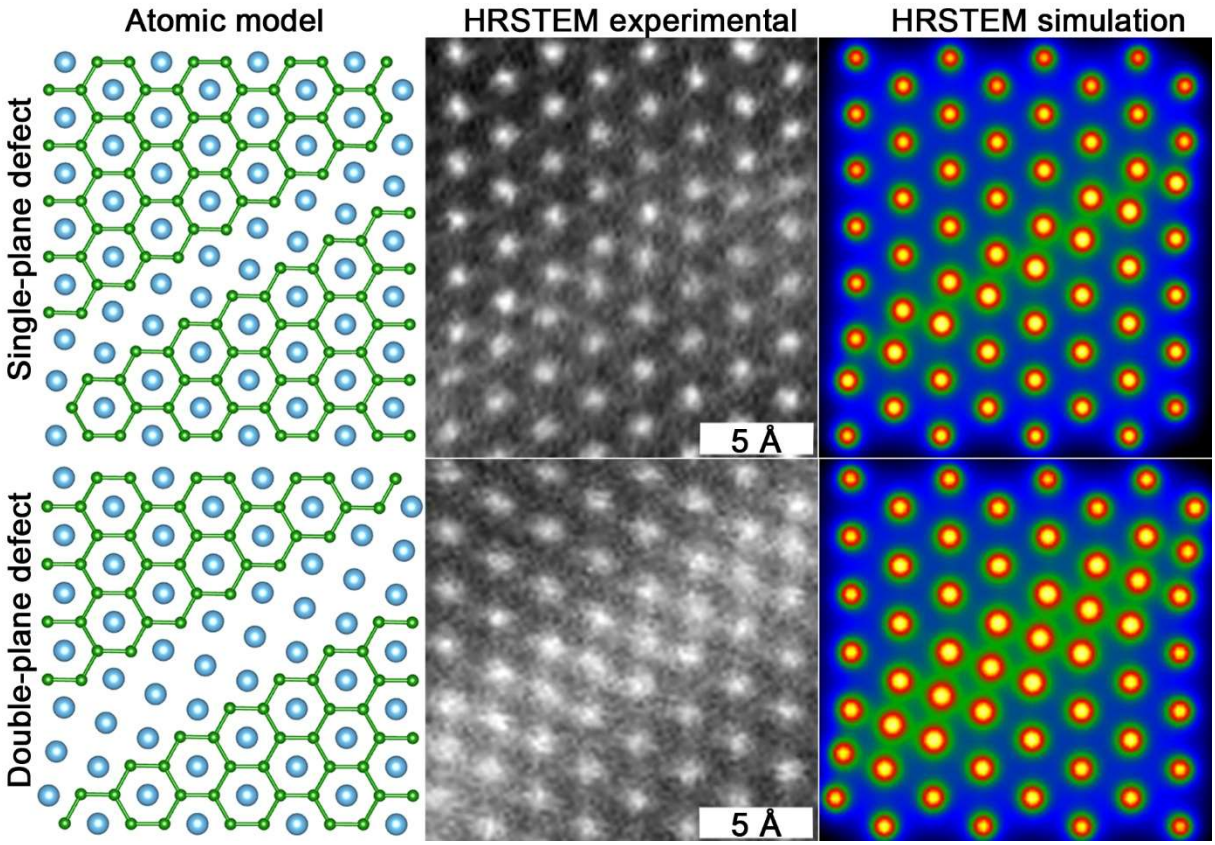

Fig. 7: *The atomic model structure, experimental and simulated HAADF-HRSTEM images of (top row) single-plane and (bottom row) double-plane defects for B vacancies viewed along the [0001] zone axis.*

The gathered experimental, theoretical and image simulation data enable us to deduce that the unmatched Ti is accommodated by the structure through the formation of Ti planar defects in the TiB_2 crystal structure.

The formation mechanism of these defects is attributed to the nature of the TiB_2 line compound, which expels surplus elements from the structure. Formation of Ti planar defects in TiB_2 can be considered as inclusions of Ti-based stacking faults within a few atomic layers, which terminates the $\{1\bar{1}00\}$ prismatic planes of the TiB_2 crystal structure. The incorporation of the Ti planar defects is driven by boron deficiency, while maintaining the TiB_2 crystal structure around the defects. In fact, this exact situation can be observed for other Ti:B compounds. TiB, e.g., forms a crystal structure (Cmcm) which exactly corresponds to TiB_2 with every 2nd B layer removed, or in Ti_3B_4 (Immm), which exactly corresponds to TiB_2 with every 3rd B layer removed [41]. TiB, Ti_3B_4, and TiB_2 are considered as stable phases (Fig. S4). The present $TiB_{1.9}$ corresponds to a situation with every 20th B layer removed (Fig. S5).

Conclusion:

High quality epitaxial thin films of substoichiometric $TiB_{1.9}$, were investigated by atomically resolved scanning transmission electron microscopy combined with DFT calculations and corresponding image simulations. We have shown that the unmatched Ti is included in the structure by formation of B-deficient planar defects residing on the $\{1\bar{1}00\}$ prismatic planes of the TiB_2 crystal structure. This mechanism to accommodate substoichiometry is attributed to the line compound nature of TiB_2, and is found to be system-universal since it enables other tested Ti:B compounds.

Acknowledgments:

The authors acknowledge the Swedish Research Council for funding under grants no. 2016-04412 and 642-2013-8020, the Knut and Alice Wallenberg's Foundation for support of the electron microscopy laboratory in Linköping, a Fellowship/Scholar grant and a project grant (KAW 2015.0043). The authors also acknowledge Swedish Foundation for Strategic Research (SSF) through the Research Infrastructure Fellow program no. RIF 14-0074. The authors also acknowledge Swedish Foundation for Strategic Research (SSF) through project funding (EM16-0004). The calculations were carried out using supercomputer resources provided by the Swedish National Infrastructure for Computing (SNIC) at the PDC Center for High Performance Computing partially funded by the Swedish Research Council through grant agreement no. 2016-07213.The authors finally acknowledge support from the Swedish Government Strategic Research Area in Materials Science on Functional Materials at Linköping University (Faculty Grant SFO-Mat-LiU No 2009 00971).

Author Contributions:

J.P. conceived the research plan with input from Iv. P. and P.O.Å.P. The materials were synthesized by A. J. H. J.P performed the experimental work related to the microscopy and data analysis. M. D. performed DFT calculations. In. P. performed image simulations. The manuscript was drafted by J.P. and finalized with input from all authors.

References:

1. R. G. Munro, *J. Res. Natl. Inst. Stand.*, 2000, **105**, 709–720

2. P. H. Mayrhofer, C. Mitterer, J. G. Wen, J. E. Greene and I. Petrov, *Appl. Phys. Lett.*, 2005, **86**, 131909

3. R. A. Andrievski, *Russ. Chem. Rev.*, 2015. **84**, 540–545

4. Y. Mu, K. Chen, W. J. Meng and F. Mei, *Microsyst. Technol.*, 2012. **18**, 667–677

5. C. Mitterer, *J. Solid State Chem.*, 1997, **133**, 279–291

6. A. Mockuté, J. Palisaitis, N. Nedfors, P. Berastegui, E. Broitman, B. Alling, L.-Å. Näslund, L. Hultman, J. Patscheider, U. Jansson, P. O.Å. Persson and J. Rosén, *Thin Solid Films*, 2019, **669**, 181–187

7. A. Mockuté, J. Palisaitis, B. Alling, P. Berastegui, E. Broitman, L.-Å. Näslund, N. Nedfors, J. Lu, J. Jensen, L. Hultman, J. Patscheider, U. Jansson, P. O.Å. Persson and J. Rosén, *Scripta Mater.*, 2017, **127**, 122–126

8. S. Ramalingam and L. S. Zheng, *Tribol. Int.*, 1995, **28**, 145–161

9. J. Neidhardt, S. Mraz, J.M. Schneider, E. Strub, W. Bohne, B. Liedke, W. Moller and C. Mitter, *J. Appl. Phys.*, 2008, **104**, 063304

10. P. J. Kelly and R.D. Arnell, *Vacuum*, 2000, **56**, 159–172

11. C.M.T.Sanchez, B. Rebollo Plata, M. E. H. Maia da Costa and F. L. Freire Jr., *Surf. Coat. Tech.*, 2011, **205**, 3698–3702

12. R. Lohmann, E. Österschulze, K. Thoma, H. Gärtner, W. Herr, B. Matthes, E. Broszeit and K.-H. Kloos, *Mat. Sci. Eng. A-Struct.*, 1991, **139**, 259–263

13. T. F. Zhang, B. Gan, S. Park, Q. M. Wang and K. H. Kim, *Surf. Coat. Tech.*, 2014, **253**, 115–122

14. N. Nedfors, A. Mockute, J. Palisaitis, P. O.Å. Persson, L.-Å. Näslund and J. Rosén, *Surf. Coat. Tech.*, 2016, **304**, 203–210

15. N. Nedfors, O. Vozniy and J. Rosén, *J. Vac. Sci. Technol. A*, 2018, **36**, 031510

16. B. Bakhit, I. Petrov, J. E. Greene, L. Hultman, J. Rosén and G. Greczynski, *Vac. Sci. Technol. A*, 2018, **36**, 030604

17. I. Zhirkov, A. Petruhins, L.-A. Naslund, S. Kolozsvári, P. Polcik and J. Rosén, *Appl. Phys. Lett.*, 2015, **107**, 184103

18. I. Zhirkov, P. Polcik, S. Kolozsvári and J. Rosén, *AIP Adv.*, 2019, **9**, 015103

19. N. Kalfagiannis, G. Volonakis, L. Tsetseris and S. Logothetidis, *J. Phys. D Appl. Phys.*, 2011, **44**, 385402

20. R. Wiedemann, H. Oettel and M. Jerenz, *Surf. Coat. Tech.*, 1997, **97**, 313–321

21. C. López-Cartes, D. Martínez-Martínez, J. C. Sánchez-López, A. Fernández, A. García-Luis, M. Brizuela and J. I. Oñate, *Thin Solid Films*, 2007, **515,** 3590–3596

22. S. K. Mishra, P. K. P. Rupa and L. C. Pathak, *Thin Solid Films*, 2007, **515**, 6884–6889

23. N. Nedfors, S. Mraz, J. Palisaitis, P. O.Å. Persson, H. Lind, S. Kolozsvari, J. M. Schneider and J. Rosén, *Surf. Coat. Tech.*, 2019, **364**, 89–98

24. N. Hellgren, J. Thörnberg, I. Zhirkov, M. A. Sortica, I. Petrov, J. E. Green, L. Hultman and J. Rosén, *Vacuum*, 2019, **169**, 108884

25. I. Petrov, F. Adibi and J. E. Greene, *J. Vac. Sci. Technol. A*, 1992, **10**, 3283–3287

26. I. Petrov, A. Hall, A. B. Mei, N. Nedfors, I. Zhirkov, J. Rosén, G. Greczynski, J. Birch, L. Hultman and J. E. Greene, *J. Vac. Sci. Technol. A*, 2017, **35**, 050601

27. J. Thörnberg, J. Palisaitis, N. Hellgren, F. Klimashin, N. Ghafoor, I. Zhirkov, C. Azina, J.-L. Battaglia, A. Kusiak, M. A. Sorica, J. E. Greene, L. Hultman, I. Petrov, P. O.Å. Persson and J. Rosén, *In manuscript*, 2020, **X**, XX–XXX

28. M. Dahlqvist, U. Jansson and J. Rosen, *J. Phys.-Condens. Mat.*, 2015, **27**, 435702

29. M. Mayer, *AIP Conf. Proc.*, 1999, **475**, 541

30. J. Barthel, *Ultramicroscopy*, 2018, **193**, 1–11

31. CrystalMaker®, CrystalMaker Software Ltd, Oxford, England (www.crystalmaker.com)

32. P.E. Blöchl, *Phys. Rev. B*, 1994, **50**, 17953–17979

33. G. Kresse and D. Joubert, *Phys. Rev. B*, 1999, **59**, 1758–1775

34. G. Kresse and J. Hafner, *Phys. Rev. B*, 1993, **47**, 558–561

35. G. Kresse and J. Furthmüller, *Comput. Mater. Sci.*, 1996, **6**, 15–50

36. G. Kresse and J. Furthmüller, *Phys. Rev. B*, 1996, **54**, 11169–11186

37. J. P. Perdew, K. Burke and M. Ernzerhof, *Phys. Rev. Lett.*, 1996, **77**, 3865–3868

38. H. J. Monkhorst and J. D. Pack, *Phys. Rev. B*, 1976, **13**, 5188–5192

39. M. Dahlqvist, B. Alling, I.A. Abrikosov and J. Rosén, *Phys. Rev. B*, 2010, **81**, 024111

40. M. Dahlqvist, B. Alling and J. Rosén, *Phys. Rev. B*, 2010, **81**, 220102

41. J. Wang, T.-N. Ye, Y. Gong, J. Wu, N. Miao, T. Tada and H. Hosono, *Nat. Commun.*, 2019, **10**, 2284